AIAA JOURNAL
Vol. 31, No. 12, December 1993

Structure of Crossing-Shock-Wave/Turbulent-Boundary-Layer Interactions

T. J. Garrison* and G. S. Settles†
Pennsylvania State University, University Park, Pennsylvania 16802
and
N. Narayanswami‡ and D. D. Knight§
Rutgers University, Piscataway, New Jersey 08903

A detailed comparison of experimental and computational results on the flowfield structure of a Mach 4, 15-deg symmetric crossing-shock-wave/turbulent-boundary-layer interaction is presented. Experimentally obtained planar laser scattering images are compared with static-pressure contours predicted by the computation, with the computational results showing good overall agreement with the experimental data. The experimental and computational results are used in a complementary manner to develop a detailed flowfield model of the crossing-shock interaction. The flowfield structure is found to consist of a complex shock structure overlying a large viscous separated region. This region occupies a significant portion of the outflow duct and consists of an accumulation of low-Mach-number, low-stagnation-pressure fluid. This region may have significant implications for sidewall compression inlets.

Introduction

THE interactions between shock waves and turbulent boundary layers are very practical propulsion-related problems, especially in association with engine inlets. These complex viscous/inviscid interactions occur in virtually all high-speed inlets and play a key role in determining the flow quality within the engine. Thus, a fundamental understanding of the physics of these interactions is critical to the design of efficient propulsion systems. Over the past 50 years a great deal of research has been directed toward understanding shock/boundary-layer interactions, its emphasis being geared toward two-dimensional and "simple" three-dimensional flows (see Ref. 1 for a thorough review of these research efforts). More recently, effort has been focused on understanding more complex, fully three-dimensional interactions. One particular example is the crossing-shock-wave/boundary-layer interaction (Fig. 1). The crossing-shock interaction is composed of the confluence of two separate single-shock interactions (for which a great deal is already known) and thus represents a logical progression in the study of shock/boundary-layer interactions. This interaction also applies to propulsion systems, since many high-speed inlets use sidewall compressions similar in geometry to the model shown in Fig. 1.

Current research on crossing-shock interactions is divided almost evenly between experimental and computational efforts. Early experimental efforts[2-6] focused mainly on characterizing the surface flow features, with emphasis on wall static pressure and surface streamline patterns. More recently, through experimental efforts researchers have gained an understanding of the overall flowfield structure and developed a physical model of these complex interactions.[7,8] Computational predictions of crossing-shock interactions have been performed by several investigators,[9,10] but until recently they have had only limited experimental data with which to compare, making a conclusive evaluation of the computations impossible. Thus, there is a need to compare the newly acquired experimental data with the computational predictions.

The goal of this paper is to present a detailed comparison of experimental and computational results for the same crossing-

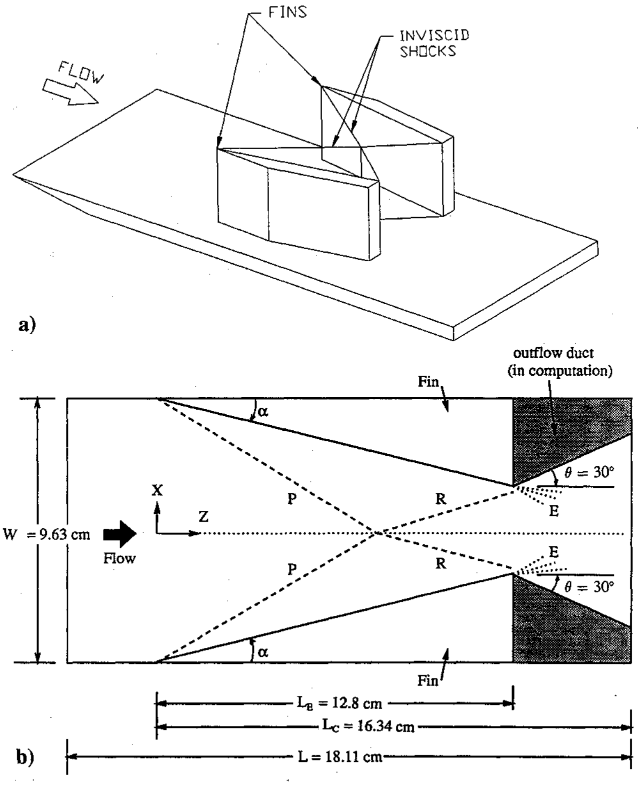

Fig. 1 Model geometry: a) perspective view of experimental geometry and b) top view of computational geometry; α = fin angle, θ = outflow duct angle (in computation only), P = primary shock, R = reflected shock, E = expansion fan, subscripts E = experiment and C = computation.

Presented as Paper 92-3670 at the AIAA/SAE/ASME/ASCE 28th Joint Propulsion Conference, Nashville, TN, July 6-8, 1992; received Nov. 5, 1992; revision received April 26, 1993; accepted for publication May 4, 1993. Copyright © 1992 by the American Institute of Aeronautics and Astronautics, Inc. All rights reserved.

*Graduate Research Assistant, Department of Mechanical Engineering. Student Member AIAA.

†Professor, Department of Mechanical Engineering, and Director, Gas Dynamics Laboratory. Associate Fellow AIAA.

‡Research Staff Member, Department of Mechanical and Aerospace Engineering; currently Research Staff, Shock Wave Research Center, Tohoku University, Sendai, Japan. Member AIAA.

§Professor, Department of Mechanical and Aerospace Engineering. Associate Fellow AIAA.

shock interaction, examining both the surface features and the flowfield structure above the surface. The objectives of this comparison are to evaluate the ability of the computation to predict the flowfield and to improve and revise the flowfield model originally presented in Ref. 7. By comparing the results of the data and the prediction, one can use the strengths of both in a complementary fashion to formulate a detailed flowfield model of the crossing-shock interaction.

Description of Experiments

The experiments were performed in the Penn State Gas Dynamics Laboratory's Supersonic Wind Tunnel Facility, which is an intermittent blowdown tunnel with a test section size of 15 × 17 × 60 cm. This facility has a unique variable Mach number capability over the range from Mach 1.5 to 4.0. For the experiments described in this paper, typical tunnel operating conditions were a stagnation pressure of 1500 kPa, a stagnation temperature of 295 K, and a unit Reynolds number of 76×10^6/m.

Figure 1a shows the model geometry used for the crossing-shock experiments. This model consists of two vertical fins, both at angle of attack α, mounted to a horizontal flat plate. The flat plate generates an equilibrium, nearly adiabatic, zero-pressure-gradient turbulent boundary layer that interacts with the two crossing oblique shock waves generated by the fins. The incoming properties of the experimental boundary layer determined from pitot surveys are $\delta \approx 3.5$ mm, $\delta^* \approx 1.12$ mm, and $\theta \approx 0.13$ mm (values revised from Ref. 7). The fins are located 21.3 cm downstream of the plate leading edge, with a transverse distance between the fin leading edges of 9.63 cm. The height of the fins is 8.25 cm, large enough to be effectively "semi-infinite."

The complete experimental program examined a range of symmetric shock generator angles ranging from 7 to 13 deg at Mach 3 and 7 to 15 deg at Mach 4. The experimental measurements consisted of surface flow visualization and planar laser scattering (PLS) flowfield visualization. PLS visualization, also referred to as laser light screen or vapor screen visualization, is a technique by which the details of a flowfield can be recorded through scattering of laser light by seed particles in the flow. A more detailed description of the experimental setup and techniques can be found in Ref. 7. A detailed comparison of the experimental PLS images and surface patterns revealed that the structure of the crossing-shock interaction was qualitatively similar over the range of interaction strengths examined in this study.[11] Thus, this paper focuses on the analysis of only one case, namely the Mach 4, 15-deg interaction, the features of this interaction being typical of all of the interactions examined experimentally.

Description of Computations

A computation of the Mach 4, 15-deg interaction was performed for the same flow conditions and incoming boundary-layer parameters as the experimental case, but with a slightly modified geometry. Referring to Fig. 1b, in the experiment the fins were terminated at a distance $z = L_E$ downstream from the fin leading edges, where L_E is the distance required for the inviscid shocks to intersect the opposite fin surfaces. To simplify the body-fitted grid system, the physical domain of the computation was modified by the addition of an outflow duct of angle $\theta = 30$ deg. The effect of this modification on the flowfield region of interest (i.e., the region surrounding the crossing shocks) is believed to be negligible, since there is supersonic flow over the entire computational domain at $z = L_E$.

The theoretical model used in the computation is the full three-dimensional mean compressible Reynolds-averaged Navier-Stokes equations in strong conservation form.[12] Turbulence is incorporated through the Baldwin-Lomax[13] algebraic eddy-viscosity model. This turbulence model is used because of its simplicity and based on reasonable performance in computing single-sharp-fin interactions.[14] The numerical algorithm employed is the hybrid explicit-implicit scheme of Knight.[15] Utilizing the symmetry of the crossing-shock interaction, one can reduce the physical domain in the computation to one-half of the experimental domain.

Boundary conditions employed for the computational domain are as follows:

1) On the inflow boundary, an incoming two-dimensional equilibrium turbulent-boundary-layer profile is prescribed to match the experiment.

2) On the fin and plate surfaces, the velocity vector and normal gradient of static pressure are set to zero. The wall temperature is set to 1.06 T_{aw} to match the experimental value.

3) On the plane of symmetry, the normal component of velocity is set to zero, as are the normal gradients of the remaining flow properties, including static pressure, temperature, and the remaining two velocity components.

4) On the top and outflow boundaries, the gradient of all flow variables is set to zero.

For simplicity in the computational solution, the fin boundary layer is taken to be turbulent from the leading edge. Although this differs from the experiment, for which the transition point occurs downstream of the leading edge, the effect of this assumption on the flowfield region of interest has been shown to be negligible in past analysis of single-fin interactions.[16,17]

Details of the computational grid used are given in Table 1. The grid spacings were selected based on previous single-fin[16,17] and crossing-shock computations[9] for which grid resolution studies were performed. A nonuniform grid spacing in the z direction is used, with the minimum grid spacing located in the region near the inviscid shock crossing. The computation was performed on a Cray Y-MP (single processor) and required approximately 32 h of CPU time.

Comparison of Results

Surface Streamline Patterns

Figure 2 shows a comparison of experimental and computational surface streamline patterns. Examination of the results given in Fig. 2 shows that upstream, near the fin leading edges, the experimental and computed patterns are quite similar. This should be expected since the interaction starts as two separate single-fin interactions for which a great deal of research has been done. Evident in both figures are the primary separation and attachment lines and the line of upstream influence. Moving downstream, differences in the two patterns become evident, especially near the interaction centerline. In the computation, the primary separation lines come together at the interaction centerline, forming a node of separation, whereas in the experimental trace the separation lines initially converge toward the centerline but then turn downstream, never actually merging together. In fact, all of the experimental traces recorded over a range of interaction

Table 1 Grid details[a]

		z direction		
N_z	$\Delta z/\delta_\infty$†	$z_{\text{in}}/\delta_\infty$	$z_{\text{out}}/\delta_\infty$	
66	0.64	−5.0	42.2	
		y direction		
N_y	$\Delta y/\delta_\infty\vert_{\min}$	$\Delta y/\delta_\infty\vert_{\max}$	$y_{\max}/\delta_\infty$	NBL
66	1.2×10^{-4}	0.58	22.9	28
		x direction		
N_x	$\Delta x/\delta_\infty\vert_{\min}$	$\Delta x/\delta_\infty\vert_{\max}$	$x_{\max}/\delta_\infty$	NBL
44	1.9×10^{-4}	0.74	13.76	20

[a] δ = boundary-layer thickness, N_x, N_y, and N_z = number of points along x, y, and z directions, respectively; Δx, Δy, and Δz = grid spacings in x, y, and z directions, respectively; subscripts in and out = at inflow and outflow planes; max = maximum; min = minimum; ∞ = evaluated in freestream; † = variable grid spacing; reported values are in the vicinity of the inviscid shock-crossing location.

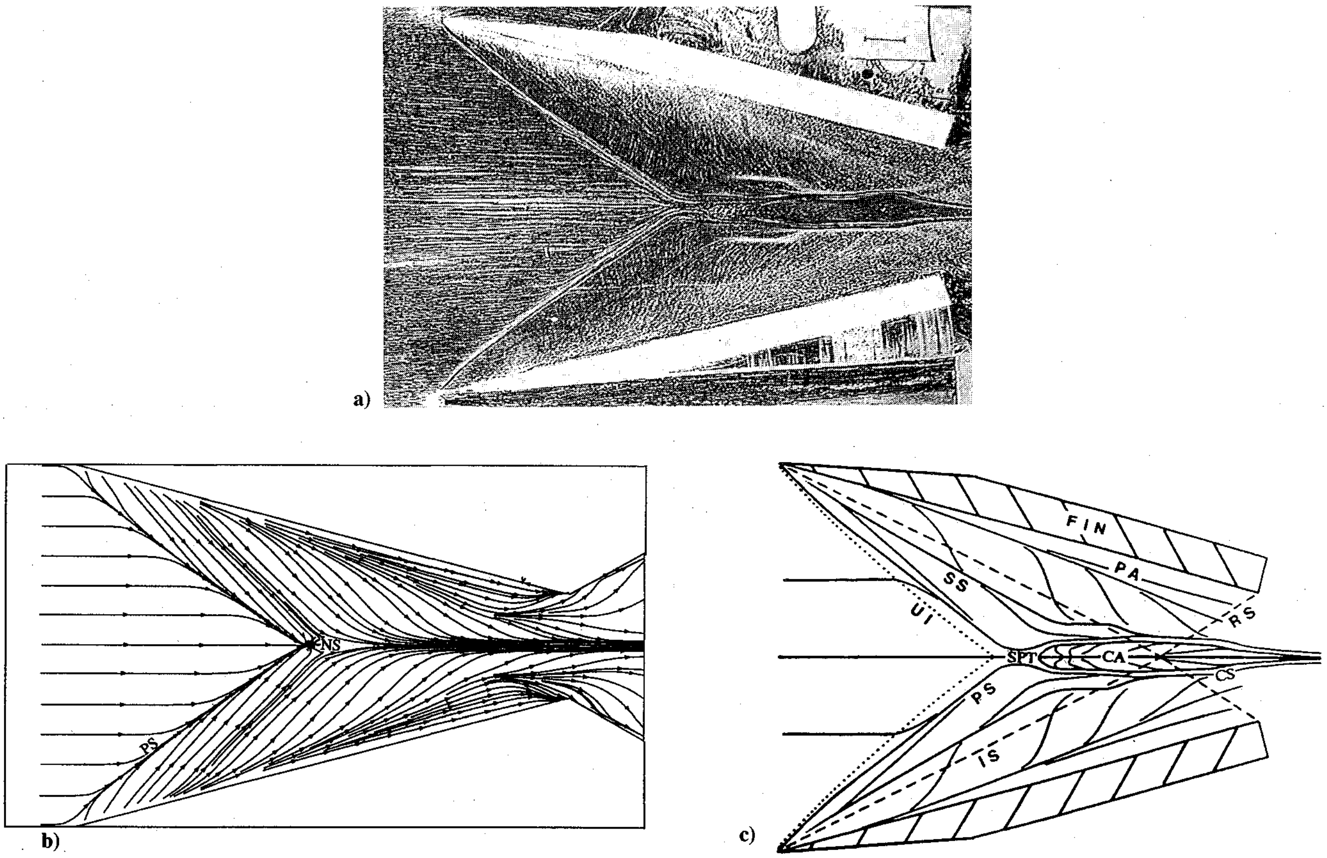

Fig. 2 Surface flow patterns: a) experimental trace, b) computational trace, and c) sketch showing key features of experimental trace; PS = primary separation, IS = inviscid shock, RS = reflected inviscid shock, UI = upstream influence, SS = secondary separation, PA = primary attachment, NS = node of separation, SPT = saddle point, CA = centerline attachment, and CS = centerline separation.

strengths showed this same behavior; the primary separation lines initially converge toward the centerline, then diverge from it, then finally approach it again further downstream. A detailed description of the experimental trace and its various topological features is given in Ref. 11.

The discrepancies in the computational and experimental patterns along the interaction centerline are most likely attributable to the inaccuracy of the Baldwin-Lomax turbulence model used in the computation. This region consists of a highly separated, vortical flowfield that is quite complex and most likely not modeled well near the surface. Away from the centerline, the computed patterns again show reasonable agreement with the experimental results. Based on a comparison of the computed and experimental flowfields above the surface, as described in the following section, it is felt that the flowfield features in the vicinity of the interaction centerline are very localized near the plate surface and do not have a significant effect on the flowfield away from the surface. However, the effects on surface properties such as skin friction and heat transfer are yet to be fully resolved. Experimental heat transfer measurements for a Mach 8.3, 15-deg interaction[8] reveal a relatively flat C_h distribution across the centerline, which may indicate that the observed features are not very significant to the surface properties either. Experimental skin friction measurements for a range of cases have recently been made at Penn State, and these results should shed more light on the significance of the surface flow features near the interaction centerline.[18]

Wave Structure

Figure 3 shows a comparison of computed values of the normalized static pressure P/P_∞ with the experimentally recorded planar laser scattering images at 14 spanwise (x-y) planes throughout the interaction (note that the gray scale for the computational results has been optimized for each frame, resulting in a variable gray scale as indicated in the legends of Fig. 3). These frames are at equally spaced intervals of $z/\delta_\infty = 1.43$ with the first frame at $z/\delta_\infty = 16.6$. The origin of the z axis is on the interaction centerline at the fin leading-edge position, as indicated in Fig. 1b. Figure 4 shows a corresponding interpretation of the key features revealed in the images of Fig. 3 and will be used as a basis for discussion of the flowfield structure. Also, shown in Fig. 5 is a schematic depicting the locations of the 14 frames relative to the model geometry. Notice that, based on the inherent symmetry of the crossing-shock interaction, only half of the actual interaction is shown in Fig. 4. Finally, much of the discussion of the shock wave structure that follows relies on the detailed analysis originally given in Ref. 7, and this reference should be consulted if additional insight is required.

Frames 1 of Figs. 3 and 4 occur upstream of where the two single-fin interactions meet and thus represent two separate single-fin interactions (see Ref. 19 for a thorough discussion of the single-fin flow structure). The main, separation, and rear shocks are visible in both the experimental and the computational results (note that, due to a restricted field of view, the PLS images do not extend all the way out to the fin surfaces). Also visible in the experimental images is the separation bubble under the bifurcated shock system, appearing as the dark region near the plate surface. This separated region does not show up well in the computed static-pressure contours but does appear clearly in the total-pressure contours, such as the one shown in Fig. 6. In general, the size and shape of the computed separated region compares quite well with the experimental results throughout the interaction. Because the static-pressure plots reveal the shock structure best, they alone are presented in frames 2–14 of Fig. 3 for brevity.

Frame 2 occurs slightly downstream of where the two separation shocks meet. To understand the confluence of these two separate single-fin interactions, it is beneficial to make use of

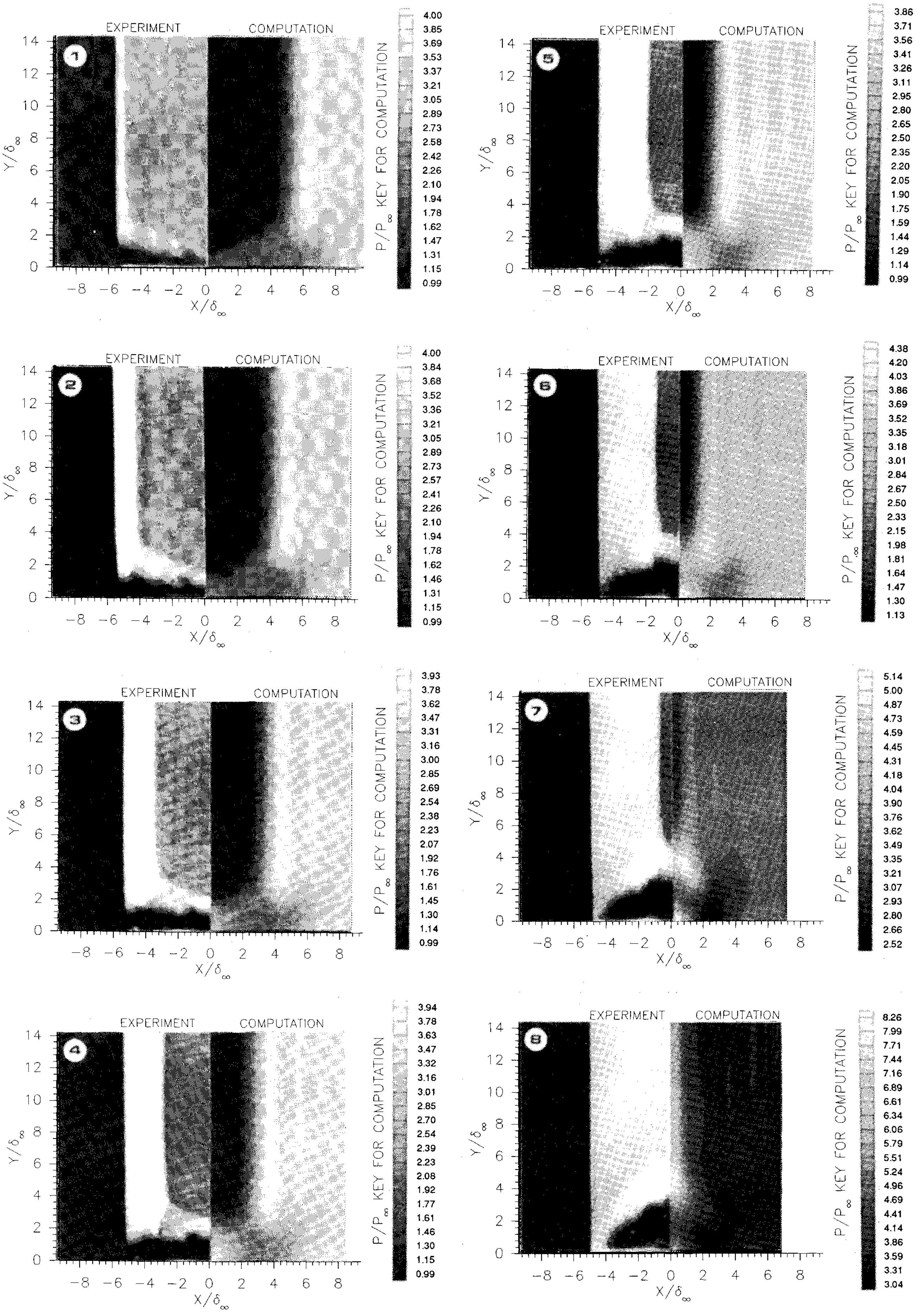

Fig. 3 Comparison of experimental PLS images with computed static pressure contours: note that numbers in the upper left give the z location as shown in Fig. 5.

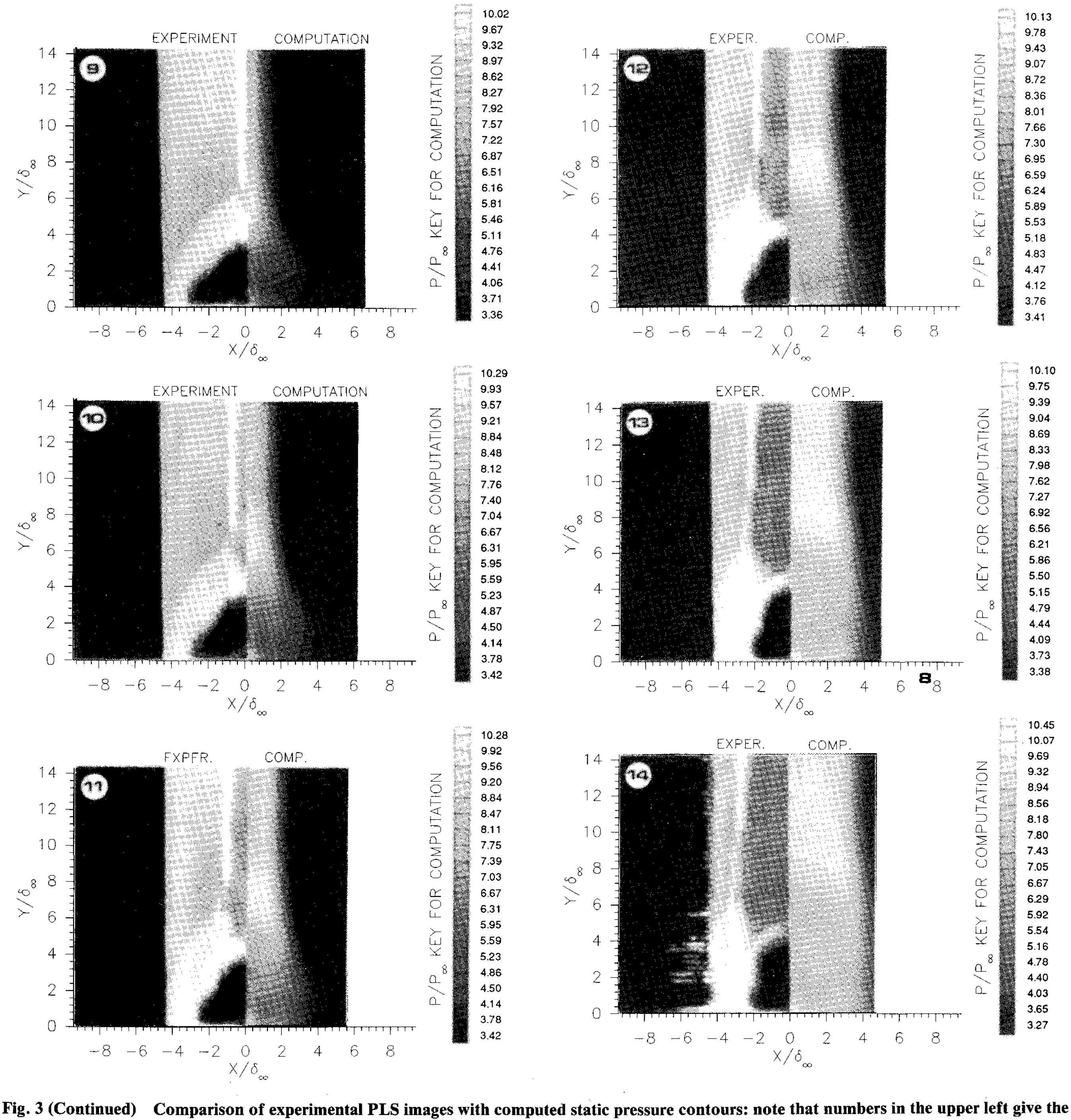

Fig. 3 (Continued) Comparison of experimental PLS images with computed static pressure contours: note that numbers in the upper left give the z location as shown in Fig. 5.

the method originally presented in Ref. 7. Here, the y-z plane passing through the interaction centerline is considered to be an inviscid reflection plane. Because of the inherent symmetry of the crossing-shock interaction, shock waves that intersect this plane must reflect from it to satisfy continuity. With this reference frame, we see that the incident separation shock reflects from the reflection plane, appearing as a bright region in the PLS images on the interaction centerline near the plate surface. The high-static-pressure region associated with this reflected separation shock can also be seen in the computational image, which coincides well with the experimental result. Careful investigation of the experimental images has revealed that the reflection of the incident separation shock is of the irregular or "Mach" variety. This Mach reflection results in a straight shock segment, the Mach stem, which spans the interaction centerline, a reflected portion of the incident separation shock, and a newly formed triple point. Frames 3–5 show that the incident separation shock continues to "reflect" from the reflection plane in an irregular manner, with the corresponding image of the shock segments in the experimental PLS images comparing quite well with the high-static-pressure region in the computation.

Frame 5 occurs approximately at the location where the reflected separation shock crosses the incident rear shock. Up to this point, the experimental and computational results compare quite well. However, beyond frame 5 a significant difference in the two results becomes evident. In the experimental PLS images of frames 6 and beyond, it is observed that the reflected separation shock crosses the incident rear shock and continues outward toward the fin, whereas in the computational results, beyond frame 5 the reflected separation shock is no longer seen (i.e., following the terminology of Fig. 4, frame 10, the reflected separation shock, item 6, is not present in the computational solution). Examination of the experimental im-

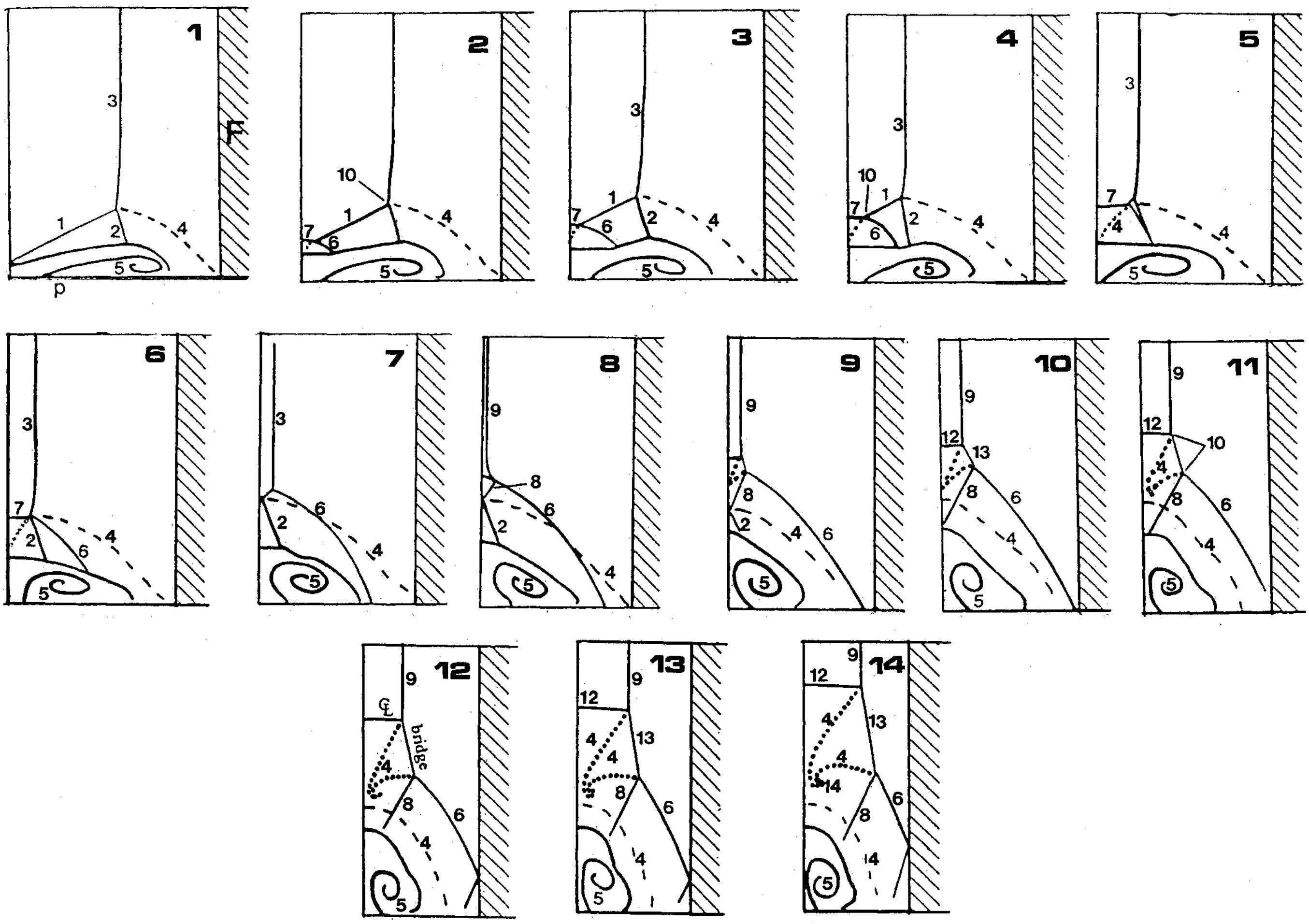

Fig. 4 Flowfield diagrams corresponding to the PLS images of Fig. 3; F = fin, p = flat plate, r = reflection plane (model centerline), 1 = incident separation shock, 2 = incident rear shock, 3 = incident "inviscid" shock, 4 = slip line, 5 = separation vortex, 6 = reflected separation shock, 7 = Mach stem, 8 = reflected rear shock, 9 = reflected "inviscid" shock, 10 = triple point, 11 = expansion, 12 = centerline shock, 13 = bridge shock, and 14 = "rolled up" slip line. Note that numbers in upper right give the z location as shown in Fig. 5.

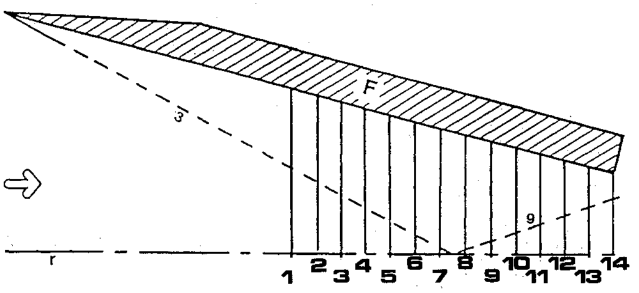

Fig. 5 Locations of frames shown in Figs. 3 and 4 relative to model geometry.

ages in Fig. 3 clearly shows the presence of the feature that has been labeled as the "main" segment of the reflected separation shock in Fig. 4. Furthermore, experimental surface flow visualization traces on the fin show the intersection of this shock wave with the fin well ahead of the location at which the inviscid shock intersects the fin, as can be seen from Fig. 7. The same pattern was observed for all interactions for which the fins were long enough to intercept the reflected wave system. Thus, it is felt that the main segment of the reflected separation shock is definitely present in the experiment but appears to be absent in the computation. Further research effort is needed to resolve this discrepancy, possibly by repeating the computation with a significantly reduced grid size.

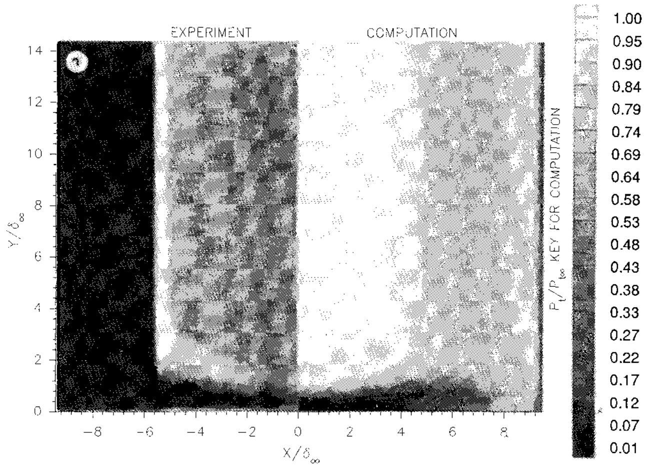

Fig. 6 Comparison of experimental PLS images with computed total pressure contour at location 1 in Fig. 5.

Next consider frame 7, which occurs just upstream of the inviscid shock-crossing location. The static-pressure plots reveal the formation of two high-pressure regions located symmetrically about the reflection plane. It is believed that these regions are associated with the complex shock crossings that occur as the two inviscid shock waves approach one another. Just below the triple point, the bifurcated shock system reflects from the reflection plane, resulting in the Mach reflection of the incident separation shock, the crossing of the reflected separation shock by the incident rear shock, and finally the reflection of the incident rear shock. This complex sequence of reflections and crossings occurs over a relatively short streamwise distance. However, at present neither the experiment nor the computation has the resolution to adequately resolve the details of this section of the interaction. Based on the experimental images taken downstream of the crossing, it is believed that the entire incident "λ-shock" structure reflects from the center plane in an irregular manner and remains intact, though somewhat distorted, propagating away from the center toward the fin surface. Current experiments are under way at Pennsylvania State University to examine the nature of the crossing region in greater detail to better understand the complex sequence of events associated with the crossing of this bifurcated shock system.

Based on the structure of the resulting flowfield downstream of the inviscid shock crossing, it appears that this process also occurs irregularly. As shown in frame 10, which occurs downstream of the location at which the reflection of the entire λ-shock system (frame 1) has been completed, two additional shock segments and two triple points are observed to form as a result of this crossing. One segment, labeled the "centerline" segment, spans the interaction centerline between the reflected inviscid shock waves, and the second, labeled the "bridge" segment, connects the reflected inviscid shock to the reflected separation and rear shocks. Thus, the entire crossing-shock interaction through frame 10 can be thought of as a complex, irregular reflection of the incident single-fin interaction at the reflection plane.

This steady, three-dimensional, irregular reflection is analogous to unsteady, two-dimensional, irregular reflections, such as those occurring in shock tube experiments. Because there is a significant amount of literature on two-dimensional irregular reflections[20,21] and very little on steady three-dimensional irregular reflections, exploiting this analogy may lead to a better understanding of the crossing-shock interaction.

In Figs. 3 and 4, frames 8 and beyond, the high-centerline-static-pressure region predicted by the computations corresponds quite well with the shock envelope comprised of the centerline and bridge shocks and the reflected rear shock (i.e., shocks labeled 6, 12, and 8). This envelope continues to grow in size as the reflected shock system moves outward toward the fin. In addition, the shape of the inviscid and bridge shock segments (9 and 13) show good agreement with the shape of the main shock structure predicted by the computation. The computation also reveals the development of an expansion region located between the two inviscid shocks, just above the separated region (this expansion is especially evident in frames 11 and beyond). This expansion cannot be seen in the experimental images because the PLS technique cannot resolve such diffuse gradients as those associated with a weak expansion.

Streamline Structure

Up to this point it has been easiest to take features found in the experimental images and find the corresponding features in the computation, simply because the spatial resolution of the PLS images is much better than that of the computation.

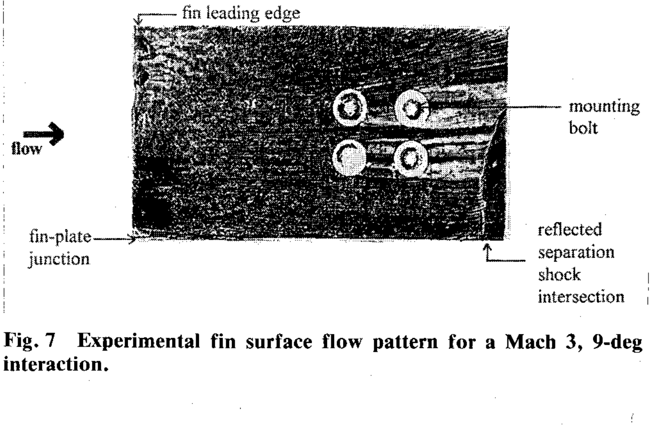

Fig. 7 Experimental fin surface flow pattern for a Mach 3, 9-deg interaction.

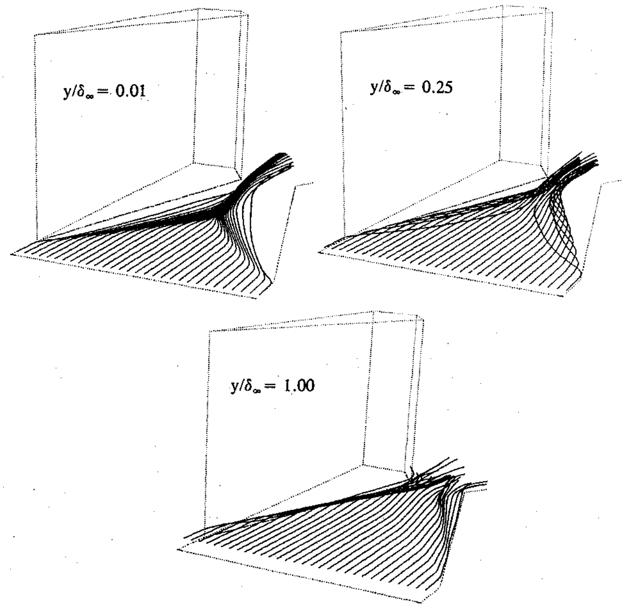

Fig. 8 Computed paths for particles released at various heights in the incoming boundary layer: a) $y/\delta_\infty = 0.01$, b) $y/\delta_\infty = 0.25$, and c) $y/\delta_\infty = 1.0$.

However, because of high temperatures and low densities that greatly reduce the seeding density, the experimental PLS images can only resolve the overall size and shape of the separated region but not the actual details within it. One expects the presence of two vortical structures (cf. Refs. 9, 14, and 19) arising from the two original single-fin interactions. Based on this expectation, the locations of the vortices within the separated region were estimated in the original flowfield model given in Ref. 7. Since the computational solution does a reasonable job of predicting the flowfield structure, it may now be used to provide additional detail in this region. It shows that the vortices are actually located closer to the plate surface than originally estimated in Ref. 7. The cores of these vortices appear clearly in the computations as two low-static-pressure regions near the plate surface. Also revealed by the computation is the presence of a very high static pressure region between these vortices. This feature also appears in the experimental PLS images, appearing as a brighter region at the plate surface near the interaction centerline. At present, the physical mechanism responsible for this high-pressure region is not completely understood.

Computational particle traces within the flowfield can also be used to help understand the flowfield streamline structure, especially within the separated region. By releasing particles at various distances from the flat plate surface within the incoming boundary layer, the flowfield streamlines can be determined. Figure 8 shows a sequence of traces for particles originating at $y/\delta_\infty = 0.01$, 0.25, and 1.0. From these traces, the formation of two counter-rotating vortices can be seen clearly. These vortices are formed beneath the two single-fin interactions and converge upon the centerline as the two interactions cross. It can also be seen that essentially the entire incoming boundary layer, along with fluid originating in the freestream, becomes engulfed in the separated region. This results in the accumulation of a large, low-Mach-number, low-stagnation-pressure region that occupies a significant portion of the outflow duct. Since the desired output of an inlet is a uniform, high-stagnation-pressure flow, this large separated-flow region has significant implications in the design of high-speed engine inlets.

Figure 8 also shows that the two vortices initially lift upward rapidly as they approach one another and then tend to "level off" further downstream. This leveling off of the streamlines within the separated region is consistent with the observation

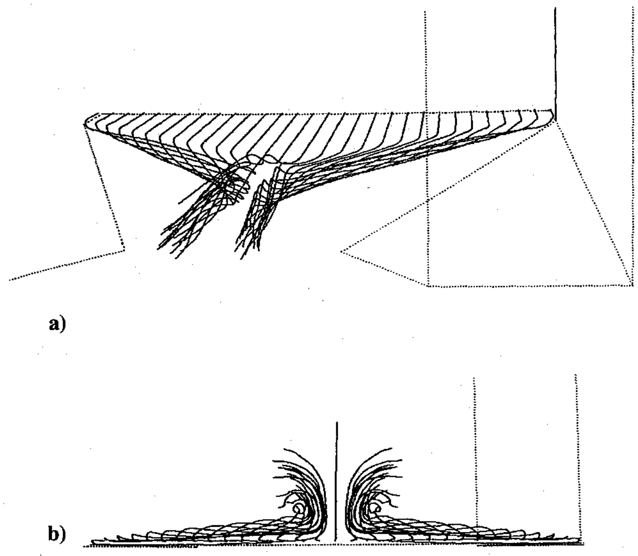

Fig. 9 Computed particle traces viewed from downstream for particles originating at $y/\delta_\infty = 0.25$: a) perspective view and b) rear view.

of the expansion above the separated region, as discussed in the previous section.

A clearer view of the twin vortices in this symmetrical interaction is shown in Fig. 9, where the particle paths seen in Fig. 8 are now viewed from downstream. In Fig. 9a the roll-up of vorticity from the entire incoming boundary layer between the fin leading edges is clearly shown to result in two concentrated vortex cores. In Fig. 9b (viewed in a direction exactly opposite to that of the freestream), the locations of these twin vortex cores are revealed.

Outside of the separated region, a new boundary layer forms through reattachment of fluid originating outside the incoming boundary layer. This new boundary layer is very thin, and so large gradients and potentially high skin friction and surface heat transfer rates may be expected (Fig. 8c).

Conclusions

The flowfield structure of a symmetric crossing-shock-wave/turbulent-boundary-layer interaction is examined both experimentally and computationally. The computation is shown to give reasonable agreement with the experimental data with two significant differences. The surface pattern predicted by the computation does not agree with the experiment in the vicinity of the interaction centerline, with the difference being attributable to the turbulence model. Also, the computation fails to resolve the presence of the main segment of the reflected separation shock. This discrepancy is not understood but may be due to resolution limits of the computation.

The results of the experiment and computation are used in a complementary manner to develop a revised model of the flowfield structure. The experiments provide good resolution of the shock structure and show that the incoming bifurcated shock structures originating from the two separate single-fin interactions cross through one another, becoming somewhat distorted, but maintaining their λ-shaped structure. The computations provide insight into the nature of the separated flow region, showing the presence of two counter-rotating vortices and the accumulation of a large, low-momentum region that may be highly detrimental to high-speed sidewall-compression inlets.

Acknowledgments

This work was supported by the Air Force Office of Scientific Research under Grants 89-0315 and 86-0266, monitored by Len Sakell. Supercomputing time was provided at the National Center for Supercomputing Applications by Cray Research Inc. through the 1992 University Research and Development Grant.

References

[1] Settles, G. S., and Dolling, D., "Swept Shock/Boundary Layer Interactions—Tutorial and Update," AIAA Paper 90-0375, Jan. 1990.

[2] Batcho, P. F., Ketchum, A. C., Bogdonoff, S. M., and Fernando, E. M., "Preliminary Study of the Interactions Caused by Crossing Shock Waves and a Turbulent Boundary Layer," AIAA Paper 89-0359, Jan. 1989.

[3] Poddar, K., and Bogdonoff, S. M., "A Study of the Unsteadiness of Crossing Shock Wave Turbulent Boundary Layer Interactions," AIAA Paper 90-1456, June 1990.

[4] Mee, D. J., Stalker, R. J., and Stollery, J. L., "Glancing Interactions Between Single and Intersecting Oblique Shock Waves and a Turbulent Boundary Layer," *Journal of Fluid Mechanics,* Vol. 170, Sept. 1986, pp. 411–433.

[5] Hingst, W. R., and Williams, K. E., "Interaction of Two Glancing, Crossing Shock Waves with Turbulent Boundary Layers at Various Mach Numbers," NASA TM 103740, 1991.

[6] Bogdonoff, S. M., and Stokes, W. L., "Crossing Shock Wave Turbulent Boundary Layer Interactions—Variable Angle and Shock Generator Length Geometry Effects at Mach 3," AIAA Paper 92-0636, Jan. 1992.

[7] Garrison, T. J., and Settles, G. S., "Flowfield Visualization of Crossing Shock-Wave/Boundary Layer Interactions," AIAA Paper 92-0750, Jan. 1992.

[8] Kussoy, M. I., and Horstman, K. C., "Intersecting Shock-Wave/Turbulent Boundary-Layer Interactions at Mach 8.3," NASA TM 103909, Feb. 1992.

[9] Narayanswami, N., Knight, D., Bogdonoff, S. M., and Horstman, C. C., "Interactions Between Crossing Oblique Shocks and a Turbulent Boundary Layer," *AIAA Journal,* Vol. 30, No. 8, 1992, pp. 1945–1952.

[10] Reddy, D. R., "3-D Navier-Stokes Analysis of Crossing, Glancing Shocks/Turbulent Boundary Layer Interactions," AIAA Paper 91-1758, June 1991.

[11] Garrison, T. J., and Settles, G. S., "Interaction Strength and Model Geometry Effects on the Structure of Crossing-Shock Wave/Turbulent Boundary-Layer Interactions," AIAA Paper 93-0780, Jan. 1993.

[12] Rubesin, M., and Rose, W., "The Turbulent Mean Flow Reynolds-Stress and Heat Flux Equations in Mass Averaged Dependent Variables," NASA TMX 62248, March 1973.

[13] Baldwin, B., and Lomax, H., "Thin Layer Approximation and Algebraic Model for Separated Turbulent Flows," AIAA Paper 78-257, Jan. 1978.

[14] Narayanswami, N., Knight, D. D., and Horstman, C. C., "Investigation of a Hypersonic Shock Wave/Turbulent Boundary Layer Interaction," *Shock Waves* (to be published).

[15] Knight, D., "A Hybrid Explicit-Implicit Numerical Algorithm for the Three Dimensional Compressible Navier-Stokes Equations," *AIAA Journal,* Vol. 22, No. 8, 1984, pp. 1056–1061.

[16] Knight, D. D., Horstman, C. C., and Monson, D. J., "The Hypersonic Shock Wave-Turbulent Boundary Layer Interaction Generated by a Sharp Fin at Mach 8.2," AIAA Paper 92-0747, Jan. 1992.

[17] Knight, D. D., and Badekas, D., "On the Quasi-Conical Flowfield Structure of the Swept Shock Wave-Turbulent Boundary Layer Interaction," AIAA Paper 91-1759, June 1991.

[18] Garrison, T. J., and Settles, G. S., "Laser Interferometer Skin-Friction Measurements of Crossing-Shock Wave/Turbulent Boundary Layer Interactions," AIAA Paper 93-3072, July 1993.

[19] Alvi, F. S., and Settles, G. S., "Physical Model of the Swept Shock/Boundary-Layer Interaction Flowfield," *AIAA Journal,* Vol. 30, No. 9, 1992, pp. 2252–2258.

[20] Ben-Dor, G., *Shock Wave Reflection Phenomena,* Springer-Verlag, New York, 1992.

[21] Hornung, H. G., "Regular and Mach Reflection of Shock Waves," *Annual Review of Fluid Mechanics,* Vol. 18, 1986, pp. 33–58.